Progress In Electromagnetics Research Letters, Vol. 131, 68–75, 2026

PIER Letters

(Received 11 July 2026, Accepted 10 August 2026, Scheduled 17 September 2026)

Design of Triple-Band High-Absorption Electromagnetic Absorber Based on Bandpass Frequency Selective Surface

Pengzhe Feng, Guang Chen*, Dongxue Han, and Yufeng Yu

School of Information and Electrical Engineering, Hangzhou City University, Hangzhou 310015, China

ABSTRACT: This study proposes a triple-band high-efficiency electromagnetic absorber constructed using a lossy resonant layer, an air spacer, and a bandpass frequency-selective surface (FSS) boundary. The lossy layer adopts bent multi-section metal resonators loaded with two types of lumped resistors to generate a multi-band resonant loss, while the underlying slot-type bandpass FSS provides frequency-dependent boundary responses: it serves as a reflective boundary at the lower two absorption bands and couples with the top-layer resonance at the higher band, while retaining out-of-band transmission. The simulated results reveal effective absorption (absorptivity $> 80\%$) at 5.2–6.1 GHz, 14.5–16.0 GHz, and 20.8–22.2 GHz, with peak absorptivities of 0.92, 1.00, and 0.97, respectively. Thanks to the centrosymmetric layout, the absorber is insensitive to TE/TM polarizations and maintains stable absorption up to 30° under oblique incidence. The operating frequencies can be flexibly tuned via slot dimensions, metal line size, and resistance values. Due to its low profile and easy processing, the proposed design is suitable for stealth, radar cross-section reduction, and electromagnetic interference mitigation.

1. INTRODUCTION

Multi-band low-profile absorbing devices are in high demand for electromagnetic stealth, radar cross-section (RCS) reduction, and electromagnetic interference (EMI) suppression [1, 2]. Early metamaterial absorbers mainly operated at single or narrow frequency bands [3]. With the development of frequency selective surface theory, lumped-resistor loaded absorbers and slot-based bandpass frequency-selective surface (FSS) have become mainstream solutions for multi-band absorption [4, 5]. Various multi-band absorbing structures based on carbon materials, FSS, and broadband resonant configurations have also been extensively explored for radar stealth and antenna electromagnetic interference suppression [6–8].

Nevertheless, existing triple-band absorbers commonly suffer from large structural thickness, low operating frequency, and obvious performance degradation under oblique incidence [9, 10]. Most reported designs fail to simultaneously realize high-frequency triple-band absorption, angular robustness, and simple fabrication [11, 12]. To address the aforementioned limitations of reported triple-band absorbers, such as large structural thickness, restricted high-frequency operation, and evident performance degradation under oblique incidence, this work proposes a low-profile three-layer passive triple-band absorber consisting of a lossy resonant layer, an air spacer, and a bandpass frequency selective surface (FSS) reflective ground. The core contributions and distinctive characteristics of this design are elaborated as follows. First, a multi-segment bent metal resonator loaded with two types of lumped resistors is constructed to excite three independent resonant modes in the microwave band, achieving three discrete high-efficiency absorption bands covering the C, Ku, and K bands with peak absorptivity exceeding 92%. Second, the designed structure employs a square-loop slot bandpass FSS as a frequency-dependent boundary, which serves as a reflective boundary at two lower absorption bands and couples with the top-layer high-frequency resonance, while enabling out-of-band transmission. This frequency-selective characteristic enables flexible impedance regulation to improve absorption efficiency. Compared with fixed-impedance solid metal ground, the slot-type FSS supports more flexible impedance regulation by tuning slot dimensions, which further optimizes the overall input impedance matching. Third, the proposed dual-resistor collaborative loading strategy enables independent loss modulation for absorption bands at different frequencies, effectively suppressing mutual coupling between adjacent resonant modes. Benefiting from the fully centrosymmetric unit configuration, the absorber presents excellent polarization insensitivity for both TE and TM polarizations and maintains stable absorption performance under oblique incidence up to 30°. With advantages of low profile and easy fabrication, this work provides a feasible alternative design for multi-band electromagnetic absorption scenarios including stealth technology and radar cross-section reduction.

2. STRUCTURE CONFIGURATION AND OPERATING PRINCIPLE

2.1. Geometric Structure and Dimensions

The proposed absorber, as illustrated in Fig. 1, is stacked in three layers from top to bottom: a lossy layer on a Rogers TC350 Plus substrate, an intermediate air spacer, and a band-

* Corresponding author: Guang Chen (cheng@hzcu.edu.cn).

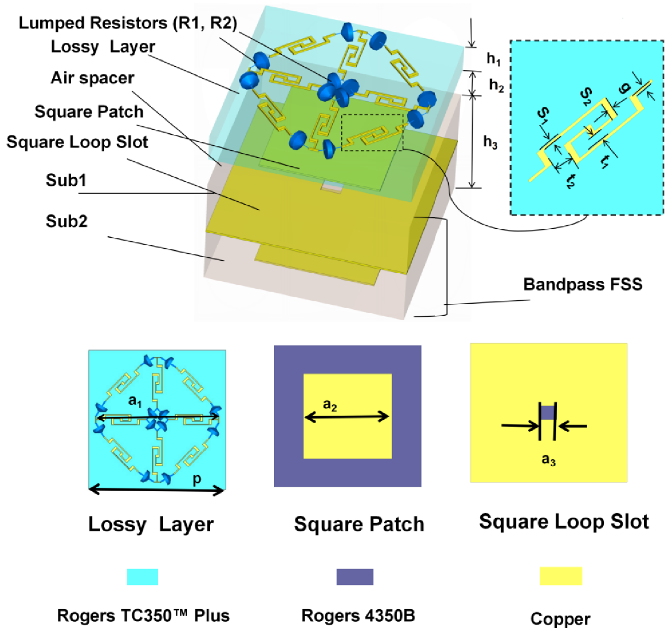

FIGURE 1. 3D exploded view of the proposed triple-band absorber.

pass FSS layer fabricated on a Rogers 4350B substrate. The unit cell has a periodicity of $P = 10\,\text{mm}$. The top substrate has a thickness $h_1 = 1.5\,\text{mm}$, a relative permittivity of 3.5, and a loss tangent of 0.0017. On the top lossy layer, the outer resonant arm has a side length $a_1 = 8\,\text{mm}$; the middle square patch has a side length $a_2 = 6\,\text{mm}$; the trace width of resonant arms is $s_1 = 0.03\,\text{mm}$; the gap between adjacent resonant arms is $g = 0.03\,\text{mm}$; and horizontal and vertical gaps inside resonant arms are $t_1 = 0.125\,\text{mm}$ and $t_2 = 0.25\,\text{mm}$, respectively. The middle air spacer has a height $h_2 = 1.5\,\text{mm}$. The bottom FSS is patterned on a Rogers 4350B substrate with thickness $h_3 = 6.1\,\text{mm}$, relative permittivity 3.66, and loss tangent 0.004; its square-loop slot has an inner side length $a_3 = 1\,\text{mm}$ and a slot width $s_2 = 0.08\,\text{mm}$. All copper metallization has a uniform thickness of 0.1 mm. Two types of lumped resistors are loaded on the resonant structure: $R_1 = 450\,\Omega$ on the outer and middle arms, and $R_2 = 150\,\Omega$ on the inner arm.

The top lossy layer consists of bent segmented copper resonators loaded with lumped resistors that consume electromagnetic power via ohmic loss. Unlike a conventional solid metal ground, the bottom bandpass FSS with square loop slots behaves as a frequency-dependent boundary: at the lower two absorption bands it reflects the incident waves back into the absorber for enhanced dissipation, while at the higher absorption band it couples with the top-layer resonance; outside the operating bands it transmits electromagnetic waves, which is the key distinction from a solid ground plane.

The equivalent inductance and capacitance of slot structures can be tailored to flexibly regulate impedance characteristics.

2.2. Working Mechanism

2.2.1. Multi-Resonance Effect

The long, medium, and short metal branches independently resonate at 5.68, 15.3, and 21.52 GHz, respectively, forming three discrete absorption peaks. R_1 dominates power dissipation at low and middle bands, whereas R_2 optimizes high-frequency absorption.

$$f_m \propto \frac{1}{\sqrt{L_m C_g}}, \tag{1}$$

where L_m is the equivalent inductance of the metal branch, and C_g is the equivalent gap capacitance. The longer the metal branch, the larger the equivalent inductance, which explains why the outermost branch corresponds to the lowest resonant frequency of 5.68 GHz, while the shortest inner branch resonates at the highest frequency of 21.52 GHz.

$$P_{\text{loss}} = \frac{1}{2} I^2 R, \tag{2}$$

where P_{loss} is the ohmic power dissipated on the lumped resistor; I is the amplitude of the induced current flowing through the resistor; and R is the resistance of the loaded lumped resistor. R_1 dominates power loss in low and middle frequency bands, while R_2 mainly adjusts the absorption intensity in the high-frequency band. With the optimal resistance configuration of $R_1 = 450\,\Omega$ and $R_2 = 150\,\Omega$, the simulated absorptivity at the three resonant points reaches 0.92, 1.00 and 0.97, respectively, verifying that the dual-resistor collaborative loading scheme achieves efficient energy dissipation in all three bands.

2.3. Impedance Matching Effect

Free-space intrinsic impedance is:

$$Z_0 = \sqrt{\frac{\mu_0}{\varepsilon_0}} \approx 377\,\Omega. \tag{3}$$

where Z_0 is the intrinsic impedance of free space; μ_0 denotes the permeability of vacuum; and ε_0 represents the permittivity of vacuum.

Absorptivity is calculated as:

$$A(\omega) = 1 - |S_{11}|^2 - |S_{21}|^2. \tag{4}$$

where $A(\omega)$ is the absorptivity at angular frequency; $|S_{11}|$ is the magnitude of the reflection coefficient; and $|S_{21}|$ is the magnitude of the transmission coefficient.

For a structure without a solid ground plane, the transmission coefficient cannot be assumed negligible a priori. In this work, the absorptivity is always calculated using the full expression in Eq. (4), i.e., $A(\omega) = 1 - |S_{11}|^2 - |S_{21}|^2$. As will be verified by the full-structure S-parameters in Fig. 2, $|S_{21}|$ remains below -10 dB across all three absorption bands, so that the transmitted power is small, and absorption is dominated by he reflection term. Nevertheless, the full expression is retained throughout for accuracy, and no simplified form is used.

By adjusting the air spacer and bandpass FSS, the absorber's input impedance is optimized to match Z_0, achieving low surface reflection [13, 14]. Full-wave simulation results show that the input impedance of the proposed structure is close to 377 Ω at 5.68 GHz, 15.3 GHz, and 21.52 GHz, which realizes excellent impedance matching and leads to near-zero reflection and peak absorption at these three frequencies.

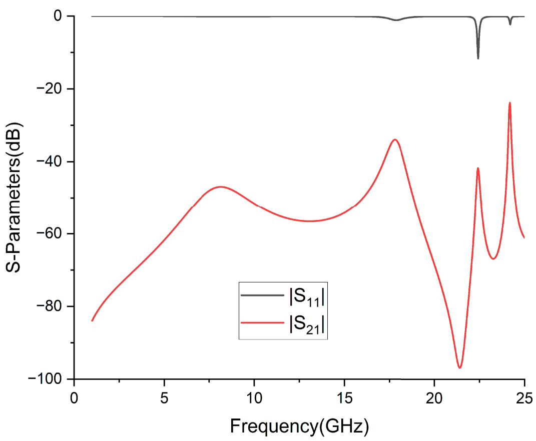

FIGURE 2. Simulated $|S_{11}|$ and $|S_{21}|$ of the standalone bandpass FSS unit cell.

2.4. Frequency-Selective Boundary Effect

The FSS's square loop slots are equivalent to LC resonant circuits:

$$f_0 = \frac{1}{2\pi\sqrt{L_{eq}C_{eq}}}, \quad (5)$$

where L_{eq} and C_{eq} are equivalent inductance and capacitance of square loop slot.

To reveal the intrinsic electromagnetic behavior of the bandpass FSS boundary, Fig. 2 shows simulated S-parameters of the standalone FSS unit cell (without the top lossy resonant layer). At the first two absorption resonances of 5.68 GHz and 15.3 GHz, the standalone FSS maintains $|S_{11}|$ close to 0 dB, indicating strong reflection. At these frequencies, the FSS acts as a frequency-selective reflective boundary: incident waves passing through the top lossy layer are reflected back for a second pass through the lossy resonator, thereby enhancing ohmic and dielectric absorption. At the third resonance near 21.52 GHz, the standalone FSS shows a deep $|S_{11}|$ dip, corresponding to its own transmissive resonance. This means that the FSS no longer behaves as a pure reflective boundary at this frequency. Instead, the third absorption peak is dominated by the strong resonant absorption of the top lossy layer itself: at 21.52 GHz, the input impedance of the lossy resonator is well matched to free space, so that most incident energy enters and is dissipated within the top layer before reaching the FSS. Consequently, even though the standalone FSS is transmissive at this frequency, the transmitted energy in the full structure remains small because the upper lossy layer has already absorbed most of the incident power. The FSS transmissive resonance couples with the top-layer resonance and jointly shapes the third absorption band. As verified by the full-structure $|S_{21}|$ curve in Fig. 2, the transmission through the whole absorber remains below -10 dB at 21.52 GHz, confirming that energy leakage is negligible. Outside target absorption bands, obvious $|S_{11}|$ dips (e.g., around 17.5 GHz and 22–24 GHz) demonstrate the FSS's inherent band-pass transmission characteristic, which distinguishes this design from conventional absorbers with a solid ground plane. By adjusting the slot dimension, the reflective and transmissive responses of the FSS can be tuned to coordinate with the three absorption bands of the top resonant layer, further improving the overall absorption efficiency [15].

Surface current distributions further verify the multi-resonance mechanism of the top lossy layer. To comprehensively validate the triple-resonance absorption mechanism, we examine the electric-field, surface-current, and power-loss distributions on the top lossy layer at the three resonant frequencies.

As shown in Fig. 3, the electric field shows distinctly different patterns at the three frequencies. At 5.68 GHz, the strong field is concentrated along the outer horizontal branches, corresponding to the fundamental resonance of the longest resonator. At 15.3 GHz, the field forms a star-like pattern concentrated at the four corners, which is characteristic of the middle-branch resonance. At 21.52 GHz, the field becomes more uniformly distributed with multiple hotspots, indicating the excitation of higher-order modes in the inner multi-segment structure [16]. These results confirm that the three absorption peaks originate from three independent resonant modes.

The surface current distributions in Fig. 4 reveal complementary information. At 5.68 GHz, the current is concentrated along the vertical middle branches, forming the inductive part of the fundamental resonance, while the electric field concentrates at the horizontal edges (capacitive part), consistent with an LC resonator. At 15.3 GHz, the current flows along the closed middle-loop structure, confirming the middle-branch resonant mode. At 21.52 GHz, the current becomes multi-directional, with X-shaped patterns, further verifying higher-order mode excitation [17]. Each subplot uses an independent color scale due to the different current magnitudes.

The power-loss distributions in Fig. 5 show that, at all three frequencies, the power loss is concentrated at the four corners where lumped resistors are loaded, confirming that the absorption is dominated by ohmic loss ($P_{\text{loss}} = I^2R$) in resistors rather than by dielectric or radiation loss. The loss distribution evolves from a rectangular pattern at 5.68 GHz (loss along the outer horizontal branches) to a corner-concentrated pattern at 15.3 GHz, and then to a slightly more dispersed pattern with weak central loss at 21.52 GHz. Each subplot uses an independent color scale due to different absolute loss magnitudes across the three frequency bands [18, 19].

Collectively, electric-field, surface-current, and power-loss distributions confirm that the three absorption peaks originate from three independent resonant modes supported by the long, medium, and short metal branches, respectively, and that the incident energy is primarily dissipated through the lumped resistors via ohmic loss.

3. SIMULATED RESULTS AND PARAMETER ANALYSIS

3.1. Absorption Performance

Full-wave simulations are carried out using CST Microwave Studio. The unit cell is simulated under normal incidence with unit-cell boundary conditions in the transverse directions and two waveguide ports at the top and bottom [20, 21]. The frequency domain solver is adopted with a hexahedral mesh, and

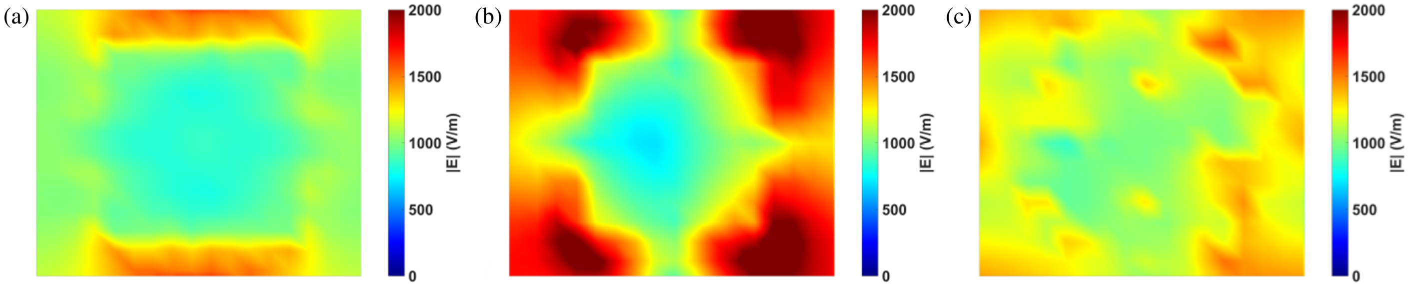

FIGURE 3. Simulated electric-field magnitude ($|E|$) distributions on the top lossy layer at (a) 5.68 GHz, (b) 15.3 GHz, and (c) 21.52 GHz.

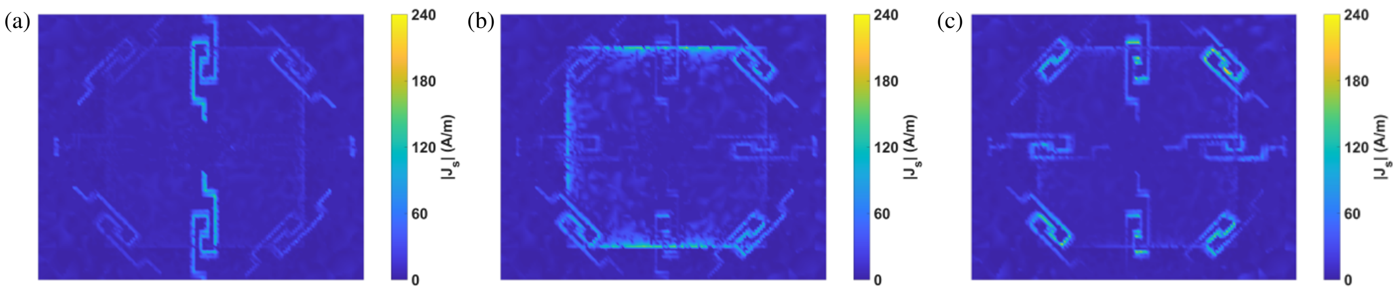

FIGURE 4. Simulated surface current density ($|J|$) distributions on the top lossy layer at (a) 5.68 GHz, (b) 15.3 GHz, and (c) 21.52 GHz.

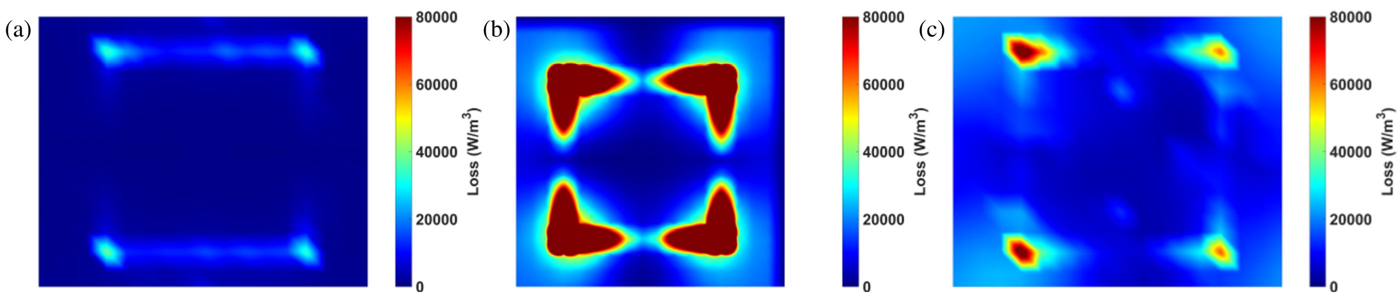

FIGURE 5. Simulated power-loss (P_{loss}) distributions on the top lossy layer at (a) 5.68 GHz, (b) 15.3 GHz, and (c) 21.52 GHz.

mesh convergence is verified by refining the mesh until the peak absorptivity variation is less than 0.5%. The copper metallization is modeled as a finite conductivity of 5.8×10^7 S/m, and the lumped resistors are implemented as lumped RLC boundary elements. The proposed design realizes three effective absorption bands (absorptivity $> 80\%$): 5.2–6.1 GHz, 14.5–16.0 GHz and 20.8–22.2 GHz, as shown in Fig. 6, with peak absorptivities of 0.92, 1.00, and 0.97 correspondingly. Half-power absorption bandwidths (absorptivity $> 50\%$) cover 4.9–6.4 GHz, 14.0–16.5 GHz and 20.3–22.7 GHz. Three absorption peaks are well separated without obvious mutual coupling, verifying the validity of multi-branch resonant design.

3.2. Angular Stability

Simulations in incident angles from 15° to 30° show slight fluctuation of absorption curves, as shown in Figs. 7 and 8. Peak absorptivity remains above 0.9 without obvious peak shift or absorption deterioration. Centrosymmetric unit layout, optimized air spacer, and stable reflective characteristic of bandpass FSS contribute to favorable angular robustness [22, 23].

3.3. Polarization Insensitivity

Due to the unit's full geometric central symmetry, the absorber shows identical absorption responses under TE- and TM-polarized incidences, realizing polarization-insensitive absorption for randomly polarized incoming waves, as shown in Fig. 9 [24, 25].

3.4. Parametric Study

3.4.1. Effect of Square Loop Slot Width

Square slot width of bandpass FSS: Enlarging slot width reduces equivalent capacitance and shifts absorption peaks to higher frequencies, while a narrower slot increases equivalent inductance to move resonances downward. As shown in Fig. 10, when the slot width varies from 0.04 mm to 0.12 mm, the first resonant peak shifts from 5.41 GHz to 5.82 GHz with peak absorptivity varying between 0.88 and 0.94; the second resonant peak shifts from 14.23 GHz to 15.61 GHz with peak absorptivity ranging from 0.95 to 1.00; the third resonant peak exhibits the most obvious frequency drift, moving from

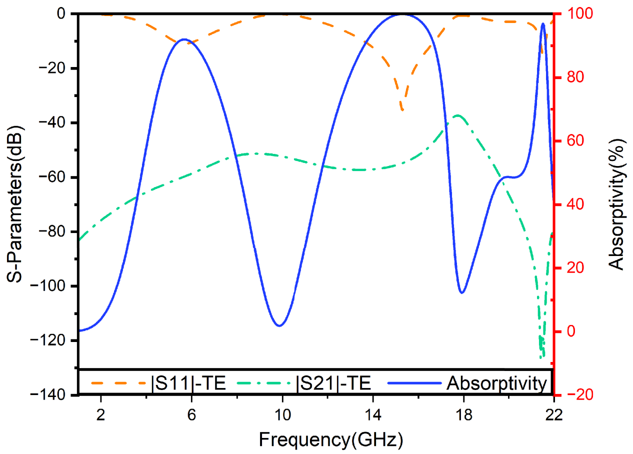

FIGURE 6. Simulated absorptivity and S-parameters of the proposed absorber.

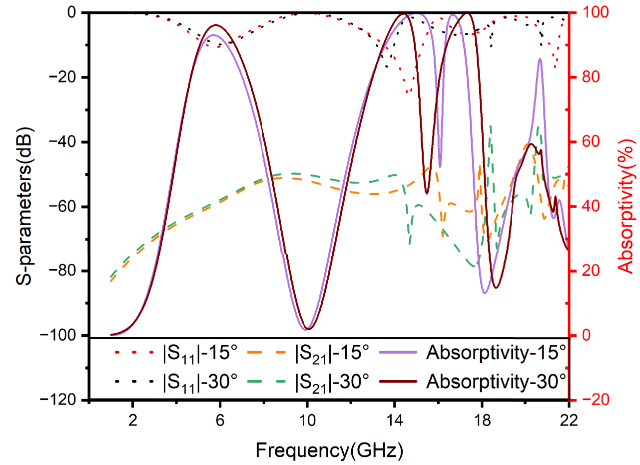

FIGURE 7. Absorption performance under 15° and 30° oblique incidence for TE polarization.

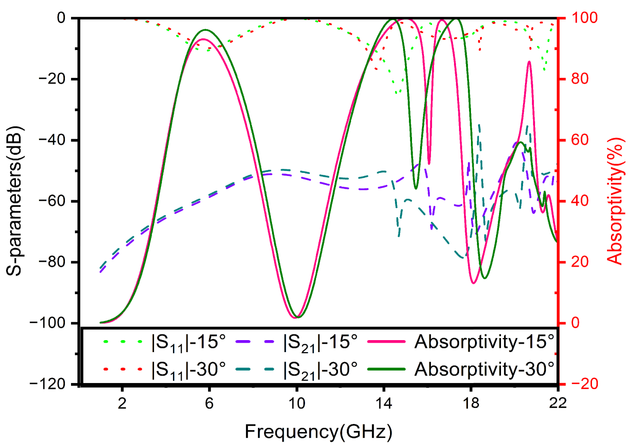

FIGURE 8. Absorption performance under 15° and 30° oblique incidence for TM polarization.

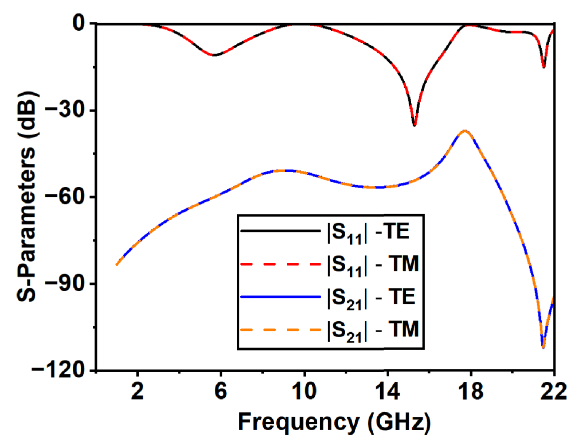

FIGURE 9. S-parameters comparison under TE and TM polarizations.

20.11 GHz to 22.03 GHz, and its peak absorptivity fluctuates within 0.91–0.98. The effective 80% absorption bandwidth for each band changes slightly within 0.7–1.0 GHz, 1.2–1.6 GHz, and 1.3–1.8 GHz, respectively. The three-band characteristic is maintained throughout parameter variation, as shown in Fig. 10 [26, 27].

3.4.2. Effect of Metal Resonator Dimension

Metal resonator dimension of lossy layer: Longer metal traces increase equivalent inductance to shift resonances to the low frequency, and shortened lines push peaks upward, enabling customized frequency assignment, as shown in Fig. 11 [28]. As the metal-resonator dimension increases from 2.2 mm to 2.8 mm, the first resonance moves downward from 5.90 GHz to 5.33 GHz; the second peak drifts from 15.72 GHz to 14.18 GHz; the third peak shifts from 22.10 GHz to 20.24 GHz. The peak absorptivity of the three bands varies within 0.89–0.95, 0.94–1.00, and 0.90–0.98, and the corresponding 80% effective absorption bandwidth varies moderately. All three absorption bands can be well distinguished within the investigated parameter range.

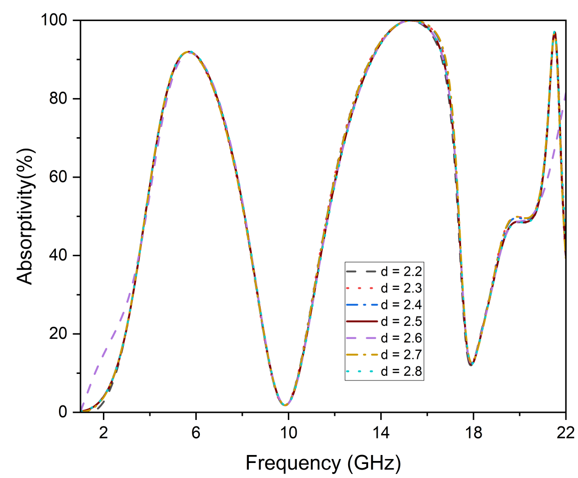

FIGURE 10. Absorption curves with different square loop slot widths (d).

3.4.3. Effect of Lumped Resistance

Lumped resistance optimization: R_1 mainly controls low- and middle-band absorption magnitude, and R_2 tunes high-frequency performance. Undervalued resistance leads to in-

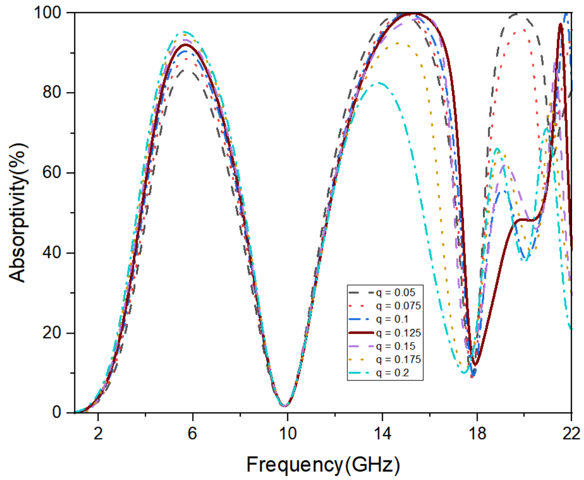

FIGURE 11. Absorption curves with different metal line dimensions (q).

sufficient loss, while excessive resistance reduces peak absorptivity; optimal resistance values are selected to balance peak level and working bandwidth, as illustrated in Fig. 12 [29, 30]. When R_1 sweeps from 300 Ω to 600 Ω, the peak absorptivity of the low band changes from 0.86 to 0.93, and the middle-band peak absorptivity varies from 0.91 to 1.00, while resonant frequencies remain almost unchanged (frequency deviation less than 0.15 GHz). When R_2 varies from 50 Ω to 300 Ω, the peak absorptivity of the high band ranges from 0.85 to 0.97, with negligible frequency shift. Under the selected optimal parameters $R_1 = 450\,\Omega$ and $R_2 = 150\,\Omega$, the absorber obtains peak absorptivities of 0.92, 1.00, and 0.97 for the three bands simultaneously.

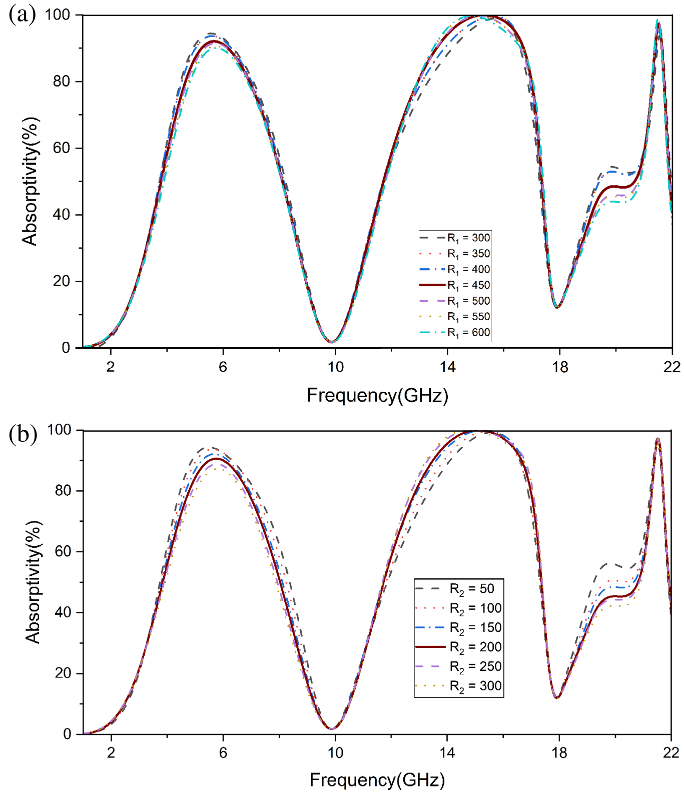

FIGURE 12. Absorptivity curves with different lumped resistances: (a) different R_1 values and (b) different R_2 values.

3.5. Performance Comparison with Reported Works

To quantitatively evaluate the proposed triple-band absorber, Table 1 summarizes a detailed comparison with five recently published related works. The referenced designs cover two typical categories: solid-metal-ground pure absorbers and frequency-selective rasorbers (FSRs), and the comparison is conducted from the perspectives of band count, operating frequency, peak absorptivity, angular stability, normalized thickness, and structural functionality.

In terms of operating band, the proposed design extends the highest absorption frequency to 22.2 GHz, covering the C, Ku, and K bands, which significantly expands the high-frequency absorption range compared with most referenced works whose upper operating limits are mainly within 12–15 GHz. For absorption performance, the peak absorptivity reaches 1.00 and 0.97 at the middle- and high-frequency bands, respectively, and remains 0.92 at the low-frequency band, meeting the requirement of high-efficiency absorption. It is worth noting that the ultra-high peak absorptivity (above 99%) in some single-layer pure absorbers corresponds to extremely narrow resonant peaks with quite limited effective bandwidth. By contrast, this work provides clear 80% absorption bandwidths for all three bands, which is more practically valuable for engineering applications.

Regarding angular stability, the proposed absorber maintains over 90% peak absorptivity within 30° oblique incidence, showing reliable performance under common incident conditions. Due to the higher operating frequency and a bandpass FSS reflective boundary, its angular stable range is narrower than that of low-frequency solid-ground absorbers. This is an inherent trade-off of the design route, and the 30° stable range still covers most conventional application scenarios. For profile thickness, the normalized thickness of the three-layer stacked structure is larger than that of single-layer pure absorbers, which is a necessary cost for introducing the air-matching layer and FSS functional layer to achieve flexible impedance tuning and out-of-band transmission. Compared with the referenced absorber, this work achieves a higher operating frequency and better high-frequency absorption with an acceptable increase in thickness.

The core innovation of the proposed design is replacing the traditional solid metal ground with a bandpass FSS. While ensuring triple-band high-efficiency absorption, it enables out-of-band wave transmission, which breaks the limitation that traditional absorbers completely block electromagnetic signals in all frequency bands. This feature makes it suitable for composite scenarios such as antenna RCS reduction and shared-aperture electromagnetic compatibility. In addition, the centrosymmetric unit layout ensures polarization insensitivity for both TE and TM polarizations, and the dual-resistor loading scheme supports flexible frequency tuning with a straightforward fabrication process. Table 1 lists detailed comparisons [6–8, 17, 22, 23].

TABLE 1. Performance comparison of triple-band FSS absorbers.

Reference	Effective Absorption Band/ Peak Frequency (GHz)	Peak Absorptivity	Polarization Stability	Angular Stability	Structural Feature
[6]	Absorptive low-reflection band: 2–12; Switchable passbands: 3.5/6/8 (dual/single-passband mode)	$>85\%$	Single polarization	0–30°	Reconfigurable multiband rasorber, loss-eliminating lossless layer, p-i-n diodes loaded
[7]	-10 dB RCS reduction band: 4.2–13.9; Dual transmission windows: 7.3/12.6	$>90\%$	Yes	0–20°	Checkerboard AMC metasurface, phase cancellation mechanism, dual transmission windows
[8]	Wideband absorption: 2.30–5.95; Band-notched mode: reflection notch at 3.5 with side absorption bands at 2.13–2.60 and 4.34–6.03	$>95\%$	Yes	0–45°	Reconfigurable absorber/reflector, p-i-ndiode loaded inductive grid, integrated bandpass/bandstop filtering
[17]	Low-reflection absorption band: 0.96–7.5; 1-dB wide passband: 3.92–4.52	$>90\%$	Yes	0–45°	Three-layer switchable rasorber, second-order inductively coupled FSS, polarization-isolated bias networke
[22]	-10 dB RCS reduction band: 5.4–14.1; Continuously tunable passband: 1.8–4.5	$>90\%$	Yes	0–30°	Varactor-tunable rasorber, coding metasurface, integrated ITO low-infrared-emissivity layer
[23]	Dual absorption bands: 6.8–7.8/12–13; Ultra-wide passband: 8.2–11.2	$>90\%$	Single polarization	0–30°	A-T-A stealth radome, lumped RLC loaded lossy layer + two cascaded lossless FSS, high-selectivity transition bands
This work	5.2–6.1/14.5–16.0/20.8–22.2 (Peak: 5.68/15.3/21.52)	$>92\%$	Yes	0–30°	Bandpass FSS + dual-resistor co-regulation, low profile

Note: Effective absorption band is defined as the frequency range with absorptivity $\geq 80\%$

4. CONCLUSION

This study designs and investigates a compact triple-band high-absorption electromagnetic absorber based on a bandpass FSS, consisting of a lossy resonant layer, an air spacer, and a bandpass FSS boundary. Multi-bent metal resonators with dual lumped resistors produce triple discrete resonant absorption. The slot-loaded bandpass FSS provides frequency-dependent boundary responses: it acts as a reflective boundary at 5.68 GHz and 15.3 GHz, and couples with the top-layer resonance at 21.52 GHz, while retaining out-of-band transmission.

The designed absorber achieves high-efficiency triple-band absorption with peak absorptivity exceeding 0.92, stable performance under 0°–30° oblique incidence, and polarization insensitivity for TE/TM waves. Tunable absorption frequency can be realized by adjusting slot size, metal line dimension, and lumped resistance. Featuring a low profile and easy fabrication, the presented absorber can be applied to electromagnetic stealth, RCS reduction, and EMI suppression, offering an effective design route for multi-band absorbing devices. This work is currently verified via full-wave simulation. Prototype fabrication and experimental measurement will be conducted in our follow-up work to further validate the proposed design.

ACKNOWLEDGEMENT

We greatly appreciate the financial support of the Baima Lake Laboratory Joint Fund of the Zhejiang Provincial Natural Science Foundation of China under Grant No. LBMHY25A040003 and the National Natural Science Foundation of China (22305216).

REFERENCES

[1] Lu, C.-Y., C.-C. Chung, T.-J. Yen, and T.-Y. Huang, "Achieving broad absorption band and high incident angles by stochastically-distributed oblique-flat-sheet metamaterial perfect absorbers," *Scientific Reports*, Vol. 11, No. 1, 18713, 2021.

[2] Munk, B. A., *Frequency Selective Surfaces: Theory and Design*, John Wiley & Sons, 2000.

[3] Kundu, D., A. Parameswaran, H. S. Sonalikar, D. Bhattacharya, and S. Gupta, "A low-RCS circularly polarized reflectarray antenna with a linearly polarized feed," *IEEE Transactions on Antennas and Propagation*, Vol. 71, No. 8, 6501–6512, 2023.

[4] Chen, J.-X., X.-F. Wang, L.-L. Yang, X.-R. Wang, X.-F. Gu, and W.-W. Yang, "Asymmetrical low-RCS FSS-based antenna for tri-band shared-aperture array," *IEEE Antennas and Wireless Propagation Letters*, Vol. 23, No. 5, 1563–1567, 2024.

[5] Wang, Z., J. Zhang, J. Hou, J. Huang, Z. Hou, M. Song, and T. A. Denidni, "Wideband and wide-angle switchable spatial filter/shielding with polarization-independent response," *IEEE An-*

tennas and Wireless Propagation Letters, Vol. 22, No. 6, 1421–1425, 2023.

[6] Peng, T., W. Huang, X. Zhou, T. Zhou, Q. Xi, and L. Yang, "Ultrathin and omnidirectional absorbing metasurface designed for electromagnetic shielding of discrete sources," *IEEE Antennas and Wireless Propagation Letters*, Vol. 23, No. 12, 4897–4901, 2024.

[7] Genikala, S., A. Ghosh, and B. Roy, "Triple band single layer microwave absorber based on closed loop resonator structures with high stability under oblique incidence," *AEU — International Journal of Electronics and Communications*, Vol. 164, 154629, 2023.

[8] Hossain, M. B., M. R. I. Faruque, M. T. Islam, M. Singh, and M. Jusoh, "Triple band microwave metamaterial absorber based on double E-shaped symmetric split ring resonators for EMI shielding and stealth applications," *Journal of Materials Research and Technology*, Vol. 18, 1653–1668, 2022.

[9] Kai, C., L. Ma, S. He, J. Zhu, and W. Huang, "Delay pre-compensation scheme for single carrier IRS-aided wideband multi-user MISO systems," *IEEE Communications Letters*, Vol. 28, No. 2, 362–366, 2024.

[10] Pati, S. S. and S. Sahoo, "Metamaterial-based angular stable polarization-insensitive hepta-band microwave absorber with salient features for RCS reduction and antenna radiation improvement," *IEEE Transactions on Electromagnetic Compatibility*, Vol. 66, No. 3, 761–775, 2024.

[11] Liu, S., R. Liu, M. Li, Y. Liu, and Q. Liu, "Joint BS-RIS-user association and beamforming design for RIS-assisted cellular networks," *IEEE Transactions on Vehicular Technology*, Vol. 72, No. 5, 6113–6128, 2023.

[12] Li, M., W. Hu, X.-X. Yang, and Z. Yi, "An ultra-wideband absorber based on mixed absorption mechanisms," *IEEE Transactions on Antennas and Propagation*, Vol. 71, No. 12, 10 009–10 013, 2023.

[13] Liao, M., X. Weng, W. Duan, K. Li, and M. Bi, "A broadband RCS reduction metasurface with dual transmission windows," *IEEE Antennas and Wireless Propagation Letters*, Vol. 23, No. 10, 3113–3117, 2024.

[14] Montofré, D., D. Meledin, C. D. Lopéz, I. Lapkin, V. Desmaris, L. Helldner, M. Fredrixon, S.-E. Ferm, and V. Belitsky, "A broad-band dual-polarization all-metal dichroic filter for cryogenic applications in sub-THz range," *IEEE Transactions on Terahertz Science and Technology*, Vol. 14, No. 2, 199–207, 2024.

[15] Chen, I., C. A. Lynch, A. Eid, J. G. D. Hester, K. Zeng, and M. M. Tentzeris, "Additively manufactured semipassive Rotman lens-based RIS-assisted mmID tag system for beyond-5G wireless networks in complex environments," *IEEE Transactions on Microwave Theory and Techniques*, Vol. 73, No. 1, 650–660, 2025.

[16] Nasser, S. S. S. and Z. N. Chen, "Low-profile broadband dual-polarization double-layer metasurface antenna for 2G/3G/LTE cellular base stations," *IEEE Transactions on Antennas and Propagation*, Vol. 70, No. 1, 75–83, 2022.

[17] Zargar, M. M., A. Rajput, K. Saurav, and S. K. Koul, "Single-layered flexible dual transmissive rasorbers with dual/triple absorption bands for conformal applications," *IEEE Access*, Vol. 9, 150 426–150 442, 2021.

[18] Negri, E., W. Fuscaldo, P. Burghignoli, and A. Galli, "Reconfigurable THz leaky-wave antennas based on innovative metal-graphene metasurfaces," *Journal of Physics D: Applied Physics*, Vol. 57, No. 48, 485102, 2024.

[19] Lienhart, M., M. Choquer, E. D. S. Nysten, M. Weiß, K. Müller, J. J. Finley, G. Moody, and H. J. Krenner, "Heterogeneous integration of superconducting thin films and epitaxial semiconductor heterostructures with lithium niobate," *Journal of Physics D: Applied Physics*, Vol. 56, No. 36, 365105, 2023.

[20] Niksan, O., K. Colegrave, and M. H. Zarifi, "Battery-free, artificial neural network-assisted microwave resonator array for ice detection," *IEEE Transactions on Microwave Theory and Techniques*, Vol. 71, No. 2, 698–709, 2023.

[21] Jiang, H., S. Liao, R. Li, and Q. Xue, "Independently switchable rasorber with wide transmission and low-reflection bands under dual polarization," *IEEE Transactions on Microwave Theory and Techniques*, Vol. 72, No. 2, 863–877, 2024.

[22] Peng, T., W. Huang, X. Zhou, F. Cai, Y. Xu, Q. Xi, Z. Huang, and L. Yang, "Triple-band and ultra-thin electromagnetic shielding absorber for discrete sources," *IEEE Antennas and Wireless Propagation Letters*, Vol. 25, No. 2, 801–805, 2026.

[23] Wang, D., Y. Zhuang, L. Shen, X. Meng, G. Wang, S. Tang, and T. Cai, "Stealth radome with an ultra-broad transparent window and a high selectivity transition band," *Optics Express*, Vol. 30, No. 10, 16 009–16 019, 2022.

[24] Zou, Y.-J., X.-W. Zhao, C. Guo, M.-D. Zhu, and Y. Zhang, "An integral equation method using periodic contact-region modeling for analyzing infinitely biperiodic composite structures," *IEEE Transactions on Antennas and Propagation*, Vol. 71, No. 7, 6237–6242, 2023.

[25] Fu, Y.-F., J.-D. Ji, Y.-J. Wang, F.-K. Zhou, C. Wang, and P. Chen, "Broadband radar cross section reduction binary metasurface with a high-efficiency intraband transmission window," *IEEE Antennas and Wireless Propagation Letters*, Vol. 21, No. 5, 878–882, 2022.

[26] Sun, M., J. Qin, M. Guan, M. Wang, X. Fu, and A. Chen, "Reconfigurable multiband rasorber with identical metallic-strip-based configuration layers for coordinated absorbing/transmitting design," *IEEE Antennas and Wireless Propagation Letters*, Vol. 22, No. 10, 2556–2560, 2023.

[27] Hu, H.-T., G.-B. Wu, K. F. Chan, and C. H. Chan, "V-band dual-polarized filtering transmitarray antenna enabled by a planar filtering illumination source," *IEEE Transactions on Antennas and Propagation*, Vol. 70, No. 10, 9184–9197, 2022.

[28] Sun, Y., J. Zhang, P. Mei, S. Luo, W. Fu, and S. Zhang, "Tri-band dual-polarized shared-aperture antenna arrays with wide-angle scanning and low profile for 5G base stations," *IEEE Transactions on Antennas and Propagation*, Vol. 72, No. 3, 2455–2467, 2024.

[29] Shukoor, M. A. and S. Dey, "Wideband via-less reconfigurable reflection and transmission linear-circular/linear-cross polarizer for vehicular satellite communication applications," *IEEE Transactions on Vehicular Technology*, Vol. 73, No. 5, 6420–6428, 2024.

[30] Shukoor, M. A. and S. Dey, "Wideband reconfigurable multifunctional absorber/reflector with bandpass/bandstop filtering and band-notch absorption for RCS and EMI shielding," *IEEE Transactions on Electromagnetic Compatibility*, Vol. 66, No. 1, 153–160, 2024.